

# Tunable plasmons in ultrathin metal films

Rinu Abraham Maniyara<sup>1,4</sup>, Daniel Rodrigo<sup>1,4</sup>, Renwen Yu<sup>1</sup>, Josep Canet-Ferrer<sup>1</sup>, Dhriti Sundar Ghosh<sup>1</sup>, Ruchirej Yongsunthon<sup>2</sup>, David E. Baker<sup>2</sup>, Aram Rezikyan<sup>2</sup>, F. Javier García de Abajo<sup>1,3\*</sup> and Valerio Pruneri<sup>1,3\*</sup>

**The physics of electrons, photons and their plasmonic interactions changes greatly when one or more dimensions are reduced down to the nanometre scale<sup>1</sup>. For example, graphene shows unique electrical, optical and plasmonic properties, which are tunable through gating or chemical doping<sup>2–5</sup>. Similarly, ultrathin metal films (UTMFs) down to atomic thickness can possess new quantum optical effects<sup>6,7</sup>, peculiar dielectric properties<sup>8</sup> and predicted strong plasmons<sup>9,10</sup>. However, truly two-dimensional plasmonics in metals has so far been elusive because of the difficulty in producing large areas of sufficiently thin continuous films. Thanks to a deposition technique that allows percolation even at 1 nm thickness, we demonstrate plasmons in few-nanometre-thick gold UTMFs, with clear evidence of new dispersion regimes and large electrical tunability. Resonance peaks at wavelengths of 1.5–5  $\mu\text{m}$  are shifted by hundreds of nanometres and amplitude-modulated by tens of per cent through gating using relatively low voltages. The results suggest ways to use metals in plasmonic applications, such as electro-optic modulation, biosensing and smart windows.**

Since ancient times, plasmons in nanoparticles of noble metals such as silver and gold have been used to colour glass, culminating during the past two decades with a remarkable broadening of the use of plasmon excitations triggered by an improved understanding of their origin and behaviour, as well as by the availability of more sophisticated means to synthesize and pattern the metals<sup>11–13</sup>. New applications promise to have an impact on the optical industry: for example, super lenses allowing unprecedented sub-diffraction-limited optical imaging<sup>14</sup>, metasurfaces providing on-chip functionality in ultrathin form factor<sup>15</sup>, light modulation<sup>16</sup>, compact biosensors<sup>17</sup> and electrochemical effects that can be used in smart windows<sup>18</sup>. All these plasmonic applications would unquestionably benefit from active electro-optic tunability. This is the case for graphene, a two-dimensional material, in which the surface carrier density ( $n_s$ ) regulating the plasmonic response can be changed by applying an external electric field (voltage)<sup>2,3</sup>. In metals, the bulk carrier density ( $n_b$ ) is large, and to change  $n_s$  significantly, one needs to achieve very small thickness ( $t$ ) values ( $n_s = n_b t$ ). The difficulty of making continuous films with sufficiently small  $t$  over a large area has so far prevented the demonstration of electro-optic tunable plasmons in metals. Here we show that, like graphene<sup>19</sup>, UTMFs with a sufficiently low nanometric thickness can support two-dimensional plasmons. In particular, we achieve dispersion and large optical tunability by electrical gating. These experiments are made possible by a new deposition technique in which copper is used as a seed layer to produce large areas of gold UTMFs. The technique (physical

vapour deposition) avoids the problem of island-like growth of unseeded gold at small thickness, giving rise to percolated films, and has the crucial advantage of being industrially scalable.

Direct evaporation of gold on substrates such as glass and other inorganic materials (for example,  $\text{CaF}_2$ ) causes the gold UTMF to grow in metallic islands of irregular shape (Volmer–Weber growth mode) during the initial growth stages owing to the poor wetting of gold<sup>20,21</sup> (Fig. 1a). The key idea introduced in our UTMF fabrication is the use of a sputtered copper seed layer with thickness  $\sim 1$  nm, which has already been shown to produce lower percolation threshold in silver films<sup>22</sup>. In this work, the copper seed layer is exposed to air and is likely to undergo oxidation before the gold evaporation (see Supplementary Notes). The resulting percolated and polycrystalline gold UTMF is shown in Fig. 1b. For a nominal thickness  $t = 3$  nm determined by extrapolation of the deposition rate, in turn calibrated by a quartz crystal microbalance, we find a roughness  $R_q = 0.22$  nm measured with atomic-force microscopy (AFM) at 3 nm lateral resolution (Fig. 1b). Long-range continuity of the seeded gold film is observed in scanning electron microscope (SEM) images at 3 nm resolution, in contrast to the disconnected geometry observed in unseeded films (Supplementary Fig. 1). We measured an average geometrical thickness of 4.42 nm using AFM for deposition of a mass-equivalent thickness  $t = 3$  nm of gold seeded by 1 nm of copper on a 285-nm-thick native silica oxide on silicon substrate (see Supplementary Fig. 2). The AFM thickness value is also consistent with scanning transmission electron microscopy (STEM) images with sub-angstrom resolution, which additionally confirm good continuity of the film (Supplementary Fig. 3). The fact that the geometrical thickness is slightly larger than the total mass-equivalent thickness (4 nm) could be due to the formation of copper oxide with a volume larger than the original metal (see Supplementary Notes for more details).

To characterize the long-range connectivity and the percolation thickness of gold UTMFs, we study visible and near-infrared transmission spectra for different  $t$  (Fig. 1c and d), as well as electrical properties (Fig. 1e). The minimum nominal (mass-equivalent) gold thickness for which a gold UTMF becomes physically connected and electrically conductive (percolation thickness) is  $t = 1$  nm and  $t = 7$  nm for seeded and unseeded growth, respectively. For  $t = 1$  nm, the seeded gold UTMF has a sheet resistance of  $\sim 1.5$  k $\Omega$  per square ( $\Omega/\square$ ), which is comparable to single-layer graphene, whereas for  $t = 3$  nm it substantially decreases to 74  $\Omega/\square$ . We also observe that for  $t \geq 3$  nm, the electrical scattering time  $\tau$  of the seeded gold UTMFs is in all cases several times smaller than in bulk metal. A full comparison of the characteristics of our UTMFs and previous results in the literature is provided in Supplementary Table 1.

<sup>1</sup>ICFO—Institut de Ciències Fotòniques, The Barcelona Institute of Science and Technology, Castelldefels (Barcelona), Spain. <sup>2</sup>Corning Research and Development Corporation, Sullivan Park, Corning, NY, USA. <sup>3</sup>ICREA—Institut Català de Recerca i Estudis Avançats, Barcelona, Spain. <sup>4</sup>These authors contributed equally: Rinu Abraham Maniyara, Daniel Rodrigo. \*e-mail: [javier.garciadeabajo@nanophotonics.es](mailto:javier.garciadeabajo@nanophotonics.es); [valerio.pruneri@icfo.eu](mailto:valerio.pruneri@icfo.eu)

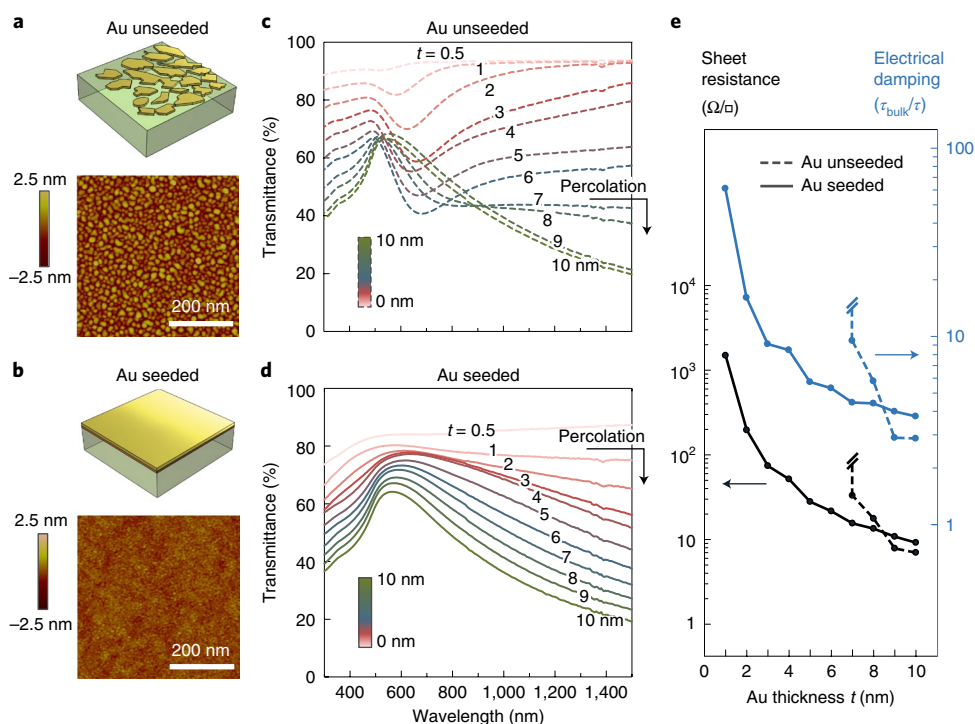


**Fig. 1 | Ultrathin metal films.** **a,b**, Conceptual view and AFM images of gold UTMFs of mass-equivalent thickness  $t \approx 3$  nm grown on 285-nm-thick native silica oxide on silicon substrates, without and with a copper seed layer. Unseeded gold (**a**) grows with discontinuous island-like morphology, whereas seeded gold (**b**) produces continuous and relatively smooth films. **c,d**, Near-infrared and visible transmission spectrum of unseeded and seeded UTMFs grown on fused silica for different gold thicknesses  $t$ . The spectra of unseeded gold UTMFs (**c**) show transmission dips at around 600 nm for  $t$  below 7 nm, corresponding to localized plasmon resonances of isolated gold islands and revealing an optically disconnected layer. In contrast, the spectra of seeded gold UTMFs (**d**) show progressively decreasing transmission at near-infrared wavelengths for  $t$  above 1 nm, demonstrating long-range connectivity. **e**, Electrical sheet resistance and damping of seeded and unseeded gold UTMFs as a function of film thickness  $t$ . Unseeded gold UTMFs are conductive only for  $t \geq 7$  nm (percolation thickness), whereas seeded UTMFs are conductive even down to  $t = 1$  nm.

The unseeded gold UTMFs present a transmission dip at approximately  $\lambda = 600\text{--}650$  nm for low coverage (Fig. 1c), which we attribute to localized optical modes as a signature of the presence of electrically isolated metallic islands<sup>23,24</sup>. For  $t \geq 7$  nm (the percolation thickness), the noted resonance starts disappearing and the transmission at longer infrared wavelengths becomes progressively lower. The measured spectra for the copper-seeded gold UTMFs (Fig. 1d) become noticeably different from the unseeded films at low coverage, in which the transmission decreases at longer wavelengths, exhibiting a typical behaviour of continuous metals down to  $t = 1$  nm, and therefore confirming a low percolation depth. In general, above percolation threshold, previous studies<sup>8,25</sup> show that the long-wavelength optical response of ultrathin gold films can be described using the Drude model with adjusted inelastic scattering rates<sup>10,26</sup> (see detailed description and comparison in Supplementary Materials). As a result of quantum confinement in the vertical direction (along the film normal), previous theoretical work showed that single-crystalline ultrathin gold films display strong anisotropy between the in-plane and out-of-plane permittivities, which might lead to a modification of the surface plasmon dispersion<sup>27,28</sup>. However, in agreement also with previous experimental studies<sup>8,29</sup>, such anisotropy does not play an important role in our experiments, because the samples are polycrystalline.

Next, we study the infrared plasmonic properties of seeded gold UTMFs with  $t$  down to 3 nm. To this end, we pattern them into nanoribbon structures of width  $W$  and period  $P$ , which enable an efficient excitation of a localized surface plasmon resonance, and specifically a first-order dipolar mode<sup>19</sup>, by illumination with normally incident infrared light (Fig. 2a). The nanostructuring of gold

UTMFs on infrared-transparent  $\text{CaF}_2$  substrates is carried out with electron beam lithography and argon reactive ion etching (Fig. 2b). We have fabricated two chips with two replicas per chip for a nominal Au thickness of 3 nm (see Supplementary Fig. 10). The resulting transmittance and reflectance for the sharper set of spectra are shown in Fig. 2c for  $t = 3$  nm,  $W$  from 200 nm to 800 nm and  $P = 1.5W$ , exhibiting strong resonances at near- and mid-infrared wavelengths. Such resonance peaks reveal that, despite the ultrathin nature of the film, the level of optical damping is low enough to support plasmonic modes. We present electromagnetic simulations in Fig. 2c (dashed curves) for comparison, obtained with a Drude damping of  $\Gamma = 0.19$  eV for 3-nm-thick gold films, although quantitatively similar results are obtained for higher values of  $\Gamma$ , so we cannot determine an accurate value for this parameter, which is several times the one for bulk metal. We remark that the plasmonic dispersion of thin films is rather independent of their detailed nanoscale morphology in the current regime of deep-subwavelength thickness (that is, porous films with a geometrical thickness up to a factor of 2 higher than the mass-equivalent thickness  $t$  would result in the same plasmon dispersion within the accuracy of the present study).

To further understand the nature of these plasmonic modes, we measured the spectral response of nano-patterned seeded gold UTMFs with mass-equivalent thicknesses  $t = 6$  nm and 15 nm (see selected spectra in Fig. 2d). We observe that for these larger thicknesses the plasmonic resonance shifts toward shorter wavelengths. This is a well-known plasmonic effect, typical of metals in the visible wavelength range<sup>10</sup>. The behaviour becomes clearer by mapping the resonance obtained from experiments into a dispersion diagram (Fig. 2e), where each point is obtained from the experimental

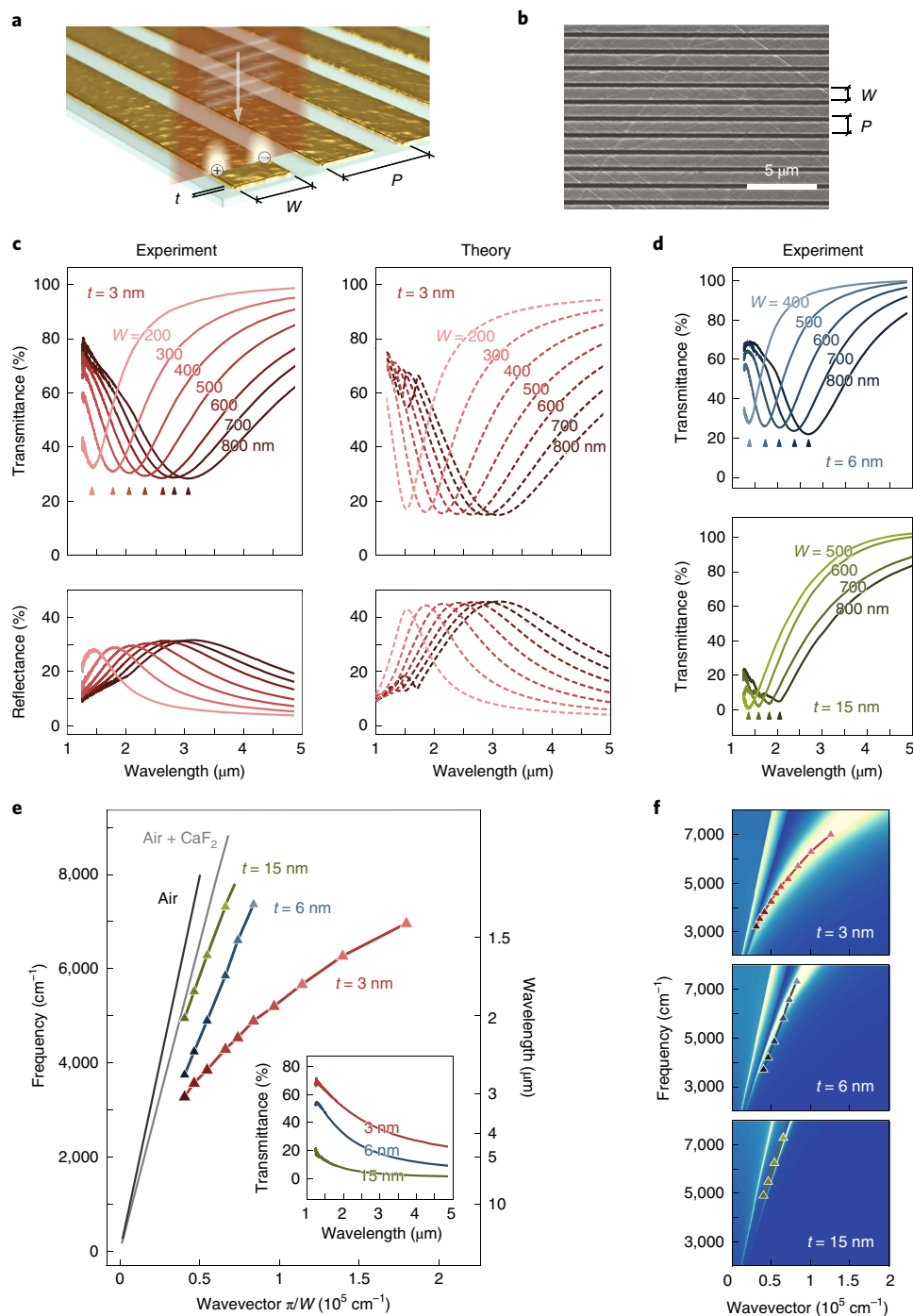


**Fig. 2 | Infrared plasmons in ultrathin metal films.** **a, b**, Conceptual view (**a**) and SEM images (**b**) of UTMF seeded gold nanoribbons of width  $W$ , period  $P$  and mass-equivalent thickness  $t$ , fabricated on  $\text{CaF}_2$  substrates. **c**, Measured and simulated spectra of selected UTMF nanoribbons showing plasmonic resonances from near- to mid-infrared for different ribbon widths  $W$  and fixed thickness  $t = 3$  nm. We use a gold Drude model with damping  $\Gamma = 0.19$  eV in the presented simulations (dashed curves). **d**, Measured transmission spectra of selected UTMF nanoribbons for  $t = 6$  nm and  $t = 15$  nm. **e**, Experimental dispersion curves of UTMF plasmons for different thicknesses obtained from the ribbon width and resonance wavelength. The thickest ribbons ( $t = 15$  nm) approach a light-line dispersion (solid grey lines), whereas the thinnest ribbons ( $t = 3$  nm) show a dispersion bending characteristic of plasmonic modes. Inset, measured transmittance spectra of continuous seeded gold UTMFs for different thicknesses. **f**, Comparison between experimental dispersion curves of UTMF plasmons and the theoretical loss function for different thicknesses. The gold Drude damping factors used in the calculations presented in the colour plots are  $\Gamma = 0.19$  eV, 0.10 eV and 0.07 eV for  $t = 3$  nm, 6 nm and 15 nm, respectively, and similar results can be obtained with larger dampings. The experimental dispersion curve is plotted using an effective wavevector  $\pi/1.25W$  (that is, using a renormalized ribbon width  $1.25W$ ) for  $t = 3$  nm.

resonance frequency of a UTMF nanoribbon array given the wave-vector condition  $k = \pi/W$  (ref. <sup>30</sup>). For large thickness ( $t = 15$  nm), the ribbon dispersion closely follows the light-line dispersion (accounting

for the surrounding refractive index). However, as the metal layer becomes thinner ( $t = 3$  nm), there is a clear dispersion bending and a deviation from the light line, which is also predicted by the

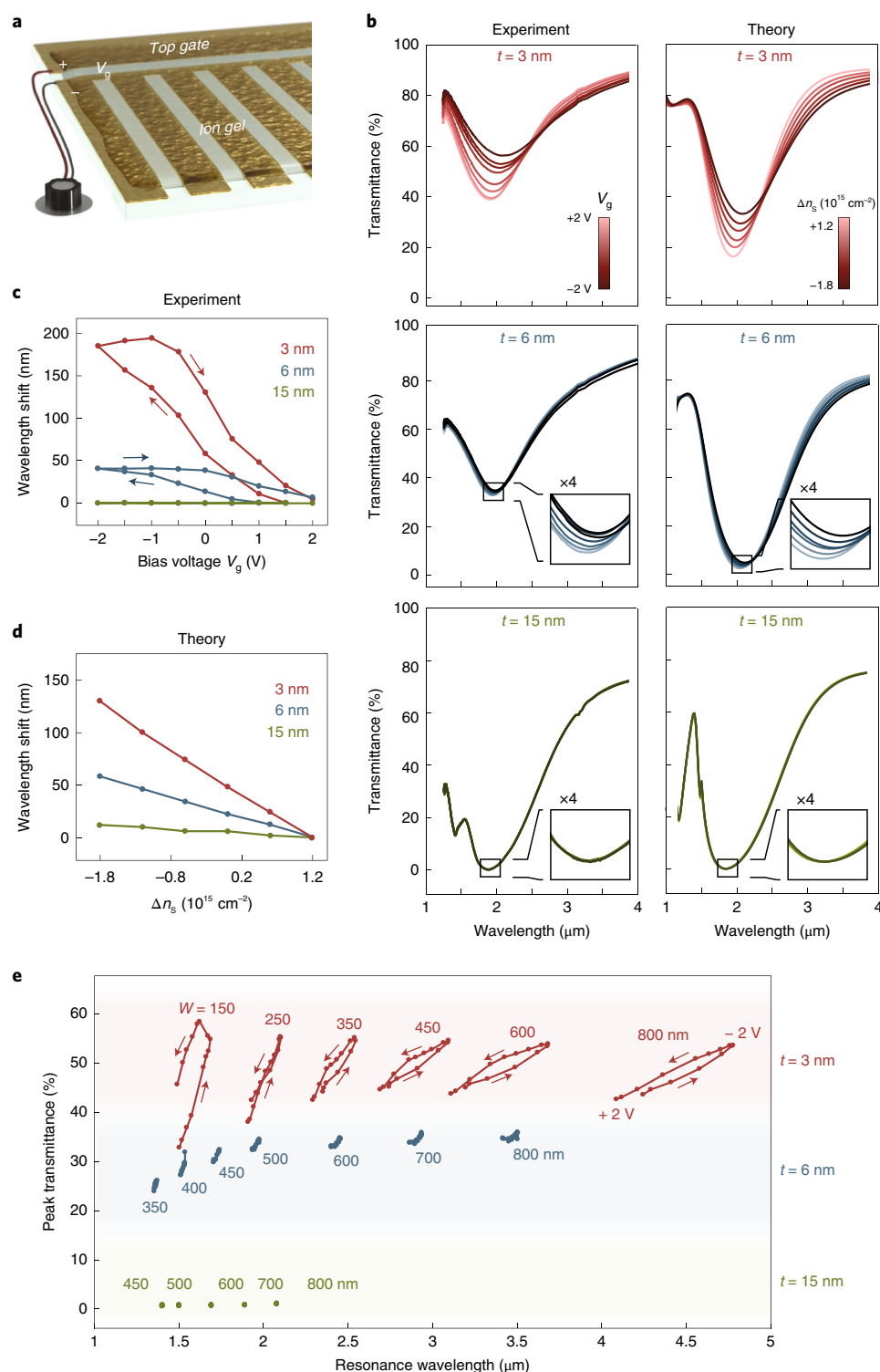


**Fig. 3 | Tunable plasmons in ultrathin metal films.** **a**, Conceptual view of the dynamic tuning of UTMF nanoribbons by ion-gel gating. **b**, Measured and simulated transmission spectra of tunable nanoribbons resonating at  $\lambda = 2 \mu\text{m}$  for thicknesses  $t = 3 \text{ nm}$ ,  $6 \text{ nm}$  and  $15 \text{ nm}$ , and widths  $W = 250 \text{ nm}$ ,  $500 \text{ nm}$  and  $700 \text{ nm}$ , respectively. The experimental spectra correspond in all cases to gating voltages  $V_g$  from  $+2 \text{ V}$  (light colour) to  $-2.0 \text{ V}$  (dark colour). The theoretical spectra correspond to nanoribbons with an effective surface charge density variation  $\Delta n_s$  between  $\Delta n_s = +1.2 \times 10^{15} \text{ carriers cm}^{-2}$  (light colour) and  $\Delta n_s = -1.8 \times 10^{15} \text{ carriers cm}^{-2}$  (dark colour). The effective surface carrier density change, used as a fitting parameter, does not necessarily correspond to a change of bulk carrier density (number of electrons per unit volume) induced in the metal. The optical damping factors  $\Gamma$  for gold used in the presented simulations vary from  $0.22 \text{ eV}$  to  $0.36 \text{ eV}$  for  $t = 3 \text{ nm}$ , and from  $0.13$  to  $0.18 \text{ eV}$  for  $t = 6 \text{ nm}$ , and are fixed at  $0.09 \text{ eV}$  for  $t = 15 \text{ nm}$ . **c**, Measured shift of the plasmonic resonance wavelength over a full voltage cycle for different gold seeded UTMF thicknesses  $t$ . **d**, Simulated shift of the plasmonic resonance wavelength by varying the effective surface carrier density  $\Delta n_s$ . Note that the wavelength shift is referred to  $\Delta n_s = +1.2 \times 10^{15} \text{ carriers cm}^{-2}$ . **e**, Measured resonance wavelength and transmission amplitude of the plasmonic peak for different thicknesses  $t$ , ribbon widths  $W$  and gating voltages  $V_g$  in the  $+2 \text{ V}$  to  $-2 \text{ V}$  range.



theoretical loss function that evaluates plasmonic energy dissipation (Fig. 2f). The bending observed in the dispersion diagram reveals the plasmonic nature of the infrared resonance modes in UTMFs when the thickness becomes sufficiently small<sup>30</sup>. Importantly, the dispersion bending takes place at metal thicknesses for which the UTMF becomes infrared-transparent (see inset in Fig. 2e), indicating that the plasmonic effects arise when the UTMF is thinner than the penetration depth of the infrared field. The physical origin of the measured plasmonic response lies in the low surface carrier density of UTMF when the thickness  $t$  becomes sufficiently small. The discrepancy in the dispersion diagram shown in Fig. 2f originates in the fact that the theoretical calculation is performed for the propagating surface plasmon modes supported in the ultrathin gold film<sup>26</sup>, which deviate from the experimental results for the localized surface plasmon modes supported in individual ribbons. After renormalization of the ribbon width, we achieve improved agreement between experiment and theory, as shown in Supplementary Fig. 9.

Next, we explore the electrical gating of plasmons in UTMFs. Considering the three-dimensional bulk carrier (free electron) density of gold  $n_b \sim 5.9 \times 10^{22} \text{ cm}^{-3}$ , its Fermi energy  $\sim 5.53 \text{ eV}$  translates into a Fermi wavelength around  $0.52 \text{ nm}$ , which is still much smaller than the minimum film thickness ( $t \sim 3 \text{ nm}$ ) studied for plasmonic response in this work. Generally, to realize a two-dimensional electron gas, one needs to maintain the condition  $n_b d^3 \ll 1$ , where  $d$  is the vertical dimension of the system (here, the film thickness). Given the large density of electrons in gold, this condition is not satisfied in our experiments, and one can use an effective surface carrier density  $n_s = n_b t$ , which has a value of  $\sim 1.8 \times 10^{16} \text{ cm}^{-2}$  for  $t = 3 \text{ nm}$ . As illustrated in Fig. 3a, the seeded gold UTMF ribbons are spin-coated with an ion gel composed of EMIM-TFSI and PS-PEO-PS polymer (see Methods) and an electrostatic voltage ( $V_g$ ) is applied between the ribbons and an external top electrode. We show in Fig. 3b (left, experiments; right, phenomenological theory) infrared spectra of selected ribbon arrays with mass-equivalent thickness  $t$  of  $3 \text{ nm}$ ,  $6 \text{ nm}$ , and  $15 \text{ nm}$  for different gate voltages from  $V_g = +2 \text{ V}$  to  $-2 \text{ V}$ . We observe in the experiments that the plasmonic resonance remains constant for  $t = 15 \text{ nm}$ , it can be slightly modulated for  $t = 6 \text{ nm}$ , and it is highly tunable for  $t = 3 \text{ nm}$ . The corresponding experimental wavelength shift is plotted in Fig. 3c and reaches  $\Delta\lambda = 200 \text{ nm}$  for  $t = 3 \text{ nm}$  and a smaller value of  $\Delta\lambda = 50 \text{ nm}$  for  $6 \text{ nm}$ , whereas for  $t = 15 \text{ nm}$  it is below the precision of experiment. The amplitude and sign of these changes depend on those of the applied voltage, and in some cases a hysteresis occurs. Similar hysteresis was observed in electrical resistance measurements of gold thin films using ion gel and low gate voltages as in our case<sup>31</sup>, which the authors attributed to oxidation/reduction of gold. This can be attributed to the inherent nature of the ionic gel (that is, a slow polarization response time of the ions, and charge trapping at the interface with the ion gel<sup>32</sup>). The wavelength shift is equivalent to a substantial change in the surface carrier density as a result of voltage gating. The effective surface carrier density change, used as a fitting parameter of the experimental results in Fig. 3, does not necessarily correspond to a change of bulk carrier density (number of electrons per unit volume) induced in the metal. For negative gating voltages there is a decrease in effective surface density of conduction electrons, which in turn produces a redshift of the plasmonic resonance. From our infrared simulations (Fig. 3d), we observe that the wavelength shifts can be explained by a maximum variation in effective surface carrier density of up to  $3 \times 10^{15} \text{ carriers cm}^{-2}$  (that is, from  $V_g = +2 \text{ V}$  to  $-2 \text{ V}$ ), which is consistent with the modulation observed in electrical transport experiments on thicker (tens of nanometres) gold films by independent groups<sup>31,33</sup>. For this maximum surface carrier density modulation, the relative variation of effective surface carrier density in our experiments is 17%, 8% and 3% in films of  $t = 3 \text{ nm}$ ,  $6 \text{ nm}$  and  $15 \text{ nm}$ , respectively, which explains the widening of the wavelength tuning range for lower UTMF

thicknesses. These modulations occur over a characteristic response time about  $1 \text{ min}$  after application of the gating potential.

In addition to the wavelength shift, there is also a modulation of the optical transmission, especially for  $t = 3 \text{ nm}$ , in which the resonance peak amplitude can be tuned from 39% to 55% transmittance. This large modulation cannot be explained by a change in surface carrier density alone. Indeed, simulations indicate that for  $t = 3 \text{ nm}$ , the variation in effective surface carrier density is responsible for less than one-quarter of the transmission modulation range (Supplementary Fig. 7). Instead, the additional mechanism dominating amplitude modulation could be associated with an effective modification of optical damping affecting the amplitude and width of the plasmonic peak. Our simulations show qualitative agreement with experiment when the Drude damping  $\Gamma$  for  $t = 3 \text{ nm}$  changes from  $0.22 \text{ eV}$  to  $0.36 \text{ eV}$  when varying the voltage  $V_g$  from  $+2 \text{ V}$  to  $-2.0 \text{ V}$ , while for  $t = 6 \text{ nm}$  we vary it from  $0.13 \text{ eV}$  to  $0.18 \text{ eV}$ . The fact that the largest damping modulation takes place for the thinnest UTMFs indicates that surface scattering may be the dominant damping channel at such small thicknesses.

We explore also the tunability of UTMFs at different wavelengths by adjusting the ribbon width  $W$ . In Fig. 3e we show the transmission amplitude and resonance wavelength of the plasmonic peak for varying voltage  $V_g$ , ribbon width  $W$  and mass-equivalent metal thickness  $t$ . For the thinnest UTMF under consideration ( $t = 3 \text{ nm}$ ) we detect tunable plasmons in the near-infrared ( $\lambda = 1.5 \mu\text{m}$ ) and in the mid-infrared ( $\lambda = 5 \mu\text{m}$ ) for the narrowest ( $W = 150 \text{ nm}$ ) and widest ( $W = 800 \text{ nm}$ ) ribbons, respectively. The transmission and wavelength tuning ranges progressively decrease as the UTMF becomes thicker. The average transmission modulation ( $\Delta T$ ) is 14.4%, 3.0% and  $<1\%$  for  $t = 3 \text{ nm}$ ,  $6 \text{ nm}$  and  $15 \text{ nm}$ , respectively. An analogous trend is found in the average wavelength tuning range ( $\Delta\lambda/\lambda_0$ ), which is 13.6%, 2.1% and  $<1\%$  for  $t = 3 \text{ nm}$ ,  $6 \text{ nm}$  and  $15 \text{ nm}$ , respectively.

Our results demonstrate plasmons in ultrathin gold films, extending the plasmonic regime to infrared wavelengths and providing a broad dynamically tunable optical response. These characteristics, combined with a large-scale fabrication approach, can find applications in transparent conductors, plasmon-enhanced spectroscopy, optical biosensing and electrochromic devices.

## Online content

Any methods, additional references, Nature Research reporting summaries, source data, statements of data availability and associated accession codes are available at <https://doi.org/10.1038/s41566-019-0366-x>.

Received: 21 August 2018; Accepted: 22 January 2019;

Published online: 25 March 2019

## References

1. Britnell, L. et al. Strong light-matter interactions in heterostructures of atomically thin films. *Science* **340**, 1311–1314 (2013).
2. Geim, A. K. & Novoselov, K. S. The rise of graphene. *Nat. Mater.* **6**, 183–191 (2007).
3. Koppens, F. H. L., Chang, D. E. & García de Abajo, F. J. Graphene plasmonics: a platform for strong light-matter interactions. *Nano Lett.* **11**, 3370–3377 (2011).
4. Liu, M. et al. A graphene-based broadband optical modulator. *Nature* **474**, 64–67 (2011).
5. Rodrigo, D. et al. Mid-infrared plasmonic biosensing with graphene. *Science* **349**, 165–168 (2015).
6. Qian, H., Xiao, Y. & Liu, Z. Giant Kerr response of ultrathin gold films from quantum size effect. *Nat. Commun.* **7**, 13153 (2016).
7. Dryzek, J. & Czapla, A. Quantum size effect in optical spectra of thin metallic films. *Phys. Rev. Lett.* **58**, 721–724 (1987).
8. Hövel, M., Gompf, B. & Dressel, M. Dielectric properties of ultrathin metal films around the percolation threshold. *Phys. Rev. B* **81**, 035402 (2010).
9. Manjavacas, A. & García de Abajo, F. J. Tunable plasmons in atomically thin gold nanodisks. *Nat. Commun.* **5**, 3548 (2014).

10. García de Abajo, F. J. & Manjavacas, A. Plasmonics in atomically thin materials. *Faraday Discuss.* **178**, 87–107 (2015).
11. Stockman, M. I. Nanoplasmonics: past, present, and glimpse into future. *Opt. Express* **19**, 22029–22106 (2011).
12. Tame, M. S. et al. Quantum plasmonics. *Nat. Phys.* **9**, 329 (2013).
13. Lu, Y., Huang, J. Y., Wang, C., Sun, S. & Lou, J. Cold welding of ultrathin gold nanowires. *Nat. Nanotechnol.* **5**, 218–224 (2010).
14. Fang, N., Lee, H., Sun, C. & Zhang, X. Sub-diffraction-limited optical imaging with a silver superlens. *Science* **308**, 534–537 (2005).
15. Nagpal, P., Lindquist, N. C., Oh, S. H. & Norris, D. J. Ultrasmooth patterned metals for plasmonics and metamaterials. *Science* **325**, 594–597 (2009).
16. Pacifici, D., Lezec, H. J. & Atwater, H. A. All-optical modulation by plasmonic excitation of CdSe quantum dots. *Nat. Photon.* **1**, 402–406 (2007).
17. Anker, J. N. et al. Biosensing with plasmonic nanosensors. *Nat. Mater.* **7**, 442–453 (2008).
18. Brown, A. M., Sheldon, M. T. & Atwater, H. A. Electrochemical tuning of the dielectric function of Au nanoparticles. *ACS Photonics* **2**, 459–464 (2015).
19. Grigorenko, A. N., Polini, M. & Novoselov, K. S. Graphene plasmonics. *Nat. Photon.* **6**, 749–758 (2012).
20. Vogt, K. W., Kohl, P. A., Carter, W. B., Bell, R. A. & Bottomley, L. A. Characterization of thin titanium oxide adhesion layers on gold: resistivity, morphology, and composition. *Surf. Sci.* **301**, 203–213 (1994).
21. Dalacu, D. & Martinu, L. Optical properties of discontinuous gold films: finite-size effects. *J. Opt. Soc. Am. B* **18**, 85–92 (2001).
22. Formica, N. et al. Ultrastable and atomically smooth ultrathin silver films grown on a copper seed layer. *ACS Appl. Mater. Interfaces* **5**, 3048–3053 (2013).
23. Jarrett, D. N. & Ward, L. Optical properties of discontinuous gold films. *J. Phys. D* **9**, 10 (1976).
24. Kreibig, U. & Vollmer, M. *Optical Properties of Metal Clusters* (Springer, 1995).
25. Brandt, T., Hövel, M., Gompf, B. & Dressel, M. Temperature- and frequency-dependent optical properties of ultrathin Au films. *Phys. Rev. B* **78**, 205409 (2008).
26. Yu, R., Pruneri, V. & García de Abajo, F. J. Active modulation of visible light with graphene-loaded ultrathin metal plasmonic antennas. *Sci. Rep.* **6**, 32144 (2016).
27. Laref, S. et al. Size-dependent permittivity and intrinsic optical anisotropy of nanometric gold thin films: a density functional theory study. *Opt. Express* **21**, 11827–11838 (2013).
28. Campbell, S. D. et al. Anisotropic permittivity of ultra-thin crystalline Au films: impacts on the plasmonic response of metasurfaces. *Appl. Phys. Lett.* **103**, 091106 (2013).
29. Kosoy, A. et al. Optical and structural properties of ultra-thin gold films. *Adv. Opt. Mater.* **3**, 71–77 (2015).
30. Yan, H. et al. Damping pathways of mid-infrared plasmons in graphene nanostructures. *Nat. Photon.* **7**, 394–399 (2013).
31. Petach, T. A., Lee, M., Davis, R. C., Mehta, A. & Goldhaber-Gordon, D. Mechanism for the large conductance modulation in electrolyte-gated thin gold films. *Phys. Rev. B* **90**, 081108 (2014).
32. Kim, J. T., Choi, H., Choi, Y. & Cho, J. H. Ion-gel-gated graphene optical modulator with hysteretic behavior. *ACS Appl. Mater. Interfaces* **10**, 1836–1845 (2018).
33. Daghero, D. et al. Large conductance modulation of gold thin films by huge charge injection via electrochemical gating. *Phys. Rev. Lett.* **108**, 066807 (2012).

## Acknowledgements

We acknowledge K. Kalavoor, M. Marchena and J. Osmond for their help in experiments and for discussions. We acknowledge financial support from the Spanish Ministry of Economy and Competitiveness through the “Severo Ochoa” programme for Centers of Excellence in R&D (SEV-2015-0522), OPTO-SCREEN (TEC2016-75080-R), and grant no. MAT2017-88492-R, from Fundació Privada Cellex, from Generalitat de Catalunya through the CERCA programme, from AGAUR 2017 SGR 1634, and from the European Union Seventh Framework Programme under grant agreement no. 609416 ICFONest. J.C.-F. also thanks MINECO for his research grant funded by means of the programme Juan de la Cierva (grant no. FPD1-2013-18078). F.J.G.A. acknowledges support from the European Research Council (Advanced Grant No. 789104-eNANO).

## Author contributions

F.J.G.A. and V.P. proposed the research project. V.P. coordinated the experiments and with the help of R.A.M. and D.R. designed them. R.A.M. and D.R. with the help of J.C.-F., D.S.G., R. Yongsunthorn, D.E.B. and A.R. carried out the experiments and characterizations. R.Yu developed the theoretical model and performed all the simulations under supervision of F.J.G.A. D.R., V.P., F.J.G.A., R. Yu and R.A.M. wrote the manuscript. All authors contributed to the interpretation of the results and manuscript writing.

## Competing interests

The authors declare no competing interests.

## Additional information

**Supplementary information** is available for this paper at <https://doi.org/10.1038/s41566-019-0366-x>.

**Reprints and permissions information** is available at [www.nature.com/reprints](http://www.nature.com/reprints).

**Correspondence and requests for materials** should be addressed to F.J.G.A. or V.P.

**Publisher's note:** Springer Nature remains neutral with regard to jurisdictional claims in published maps and institutional affiliations.

© The Author(s), under exclusive licence to Springer Nature Limited 2019

## Methods

**Deposition of UTMFs.** For characterization of the Au film and for further experiments we used different substrates, such as double-sided optically polished ultraviolet-fused silica glass substrates (with a thickness of 1 mm and an area of 1 inch square), CaF<sub>2</sub> polished window (20 mm diameter × 1 mm), and 285-nm-thick native silica oxide on silicon substrates (thickness of 500 μm). Before deposition, the substrates were cleaned in acetone followed by ethanol in ultrasonic bath, each process lasting 10 min. The substrates were then rinsed in deionized water and dried with nitrogen gas. A copper seed layer was deposited by physical vapour deposition sputtering, where the sputtering chamber was initially evacuated to a base pressure of about 10<sup>-7</sup>–10<sup>-8</sup> Torr. The target-to-substrate distance was maintained at 30 cm. The substrate holder was rotating during deposition with a speed of 60 r.p.m. Before the deposition of copper, a low-power argon plasma cleaning was performed for 15 min inside the sputtering equipment. Bias power (40 W) and pressure (8 mT) were used for cleaning in argon (20 standard cubic centimetres per minute, sccm) atmosphere. A copper sputtering target of 99.99% purity was used for depositing copper films with a d.c. power of 100 W and working pressure of 2 mTorr. Samples were exposed to air after copper deposition and before gold deposition. Gold thin films were deposited by thermal evaporation. A very small rate of deposition of about 0.1 nm s<sup>-1</sup> was chosen to increase accuracy of gold thickness using calibration techniques. The deposition rate was experimentally assessed on test samples by AFM measurements for gold thicknesses ≥ 3 nm. These measurements confirm that the deposition rate is basically constant up to a thickness of at least 30 nm (that is, the mass-equivalent thickness deposited is linear with respect to deposition time). For test samples fabricated with the same procedure as used in the thinnest UTMFs in which we measured plasmons, seeded 3 nm and 6 nm gold samples, with nominal thicknesses of 4 and 7 nm (when one considers the underlying copper seed of 1 nm), respectively, we performed AFM with a lateral resolution < 7 nm and inferred a geometrical thickness of 4.42 ± 0.14 nm and 7.40 ± 0.16 nm, respectively (the average and standard deviation values are calculated from 20 different cross-sections). The measured thicknesses are slightly larger than the nominal values, but still smaller than the expected increase in volume due to oxidation of the copper seed film (68% increase in volume from pure copper to Cu<sub>2</sub>O with the same amount of metal, which for mass-equivalent 1 nm copper and 3 nm gold would lead to 4.68 nm assuming full copper oxidation and full bulk-like packing of the materials). This discrepancy might be related to the fact that the copper is only partly oxidized. The measured thickness using AFM for seeded 3 nm gold UTMF is consistent with STEM images. Note that the thicknesses provided in the paper for all samples in which plasmons have been identified are nominal (that is, mass-equivalent) thicknesses, which are inferred from the deposition rate and time, similarly to previous works (for example, see refs. <sup>29</sup> and <sup>34</sup>).

**Nanofabrication of gold nanoribbon arrays.** Gold nanoribbon arrays were fabricated on polished CaF<sub>2</sub> substrates. Thin Au films of various thicknesses were deposited on the substrate in the same way as with fused silica according to the process flow described above. A 100 nm layer of electron beam resist (ZEP 520 A) was spin-coated over the UTMF chip. The nanoribbons were subsequently patterned in the resist with 50 keV electron beam lithography. After exposure, the resist was developed in amyl-acetate and rinsed in 9:1 MiBK:IPA solution. Next, the gold nanoribbons were etched in inductively coupled argon plasma at 300 W. Resist stripping was done in *N*-methyl-2-pyrrolidone (NMP), followed by isopropyl alcohol (IPA) and deionized water rinsing.

**Ion-gel gating of gold nanoribbon arrays.** For the gating experiments, we chose EMIM-TFSI (1-ethyl-3-methylimidazolium bis(trifluoromethylsulfonyl) imide) as the ionic liquid, similar to ref. <sup>35</sup>. A 0.56 g amount of ionic liquid was first dried under vacuum and then in a glove box for 3 days. It was then dissolved with 22 mg of PS-PEO-PS triblock copolymer in 2 ml of dry dichloromethane. The ion gel was spin-coated over the gold nanoribbons at 2,000 r.p.m. for 1 min. A top gate voltage between -2 V and +2 V was applied to the ribbon arrays. An external gate with a surface area much larger than that of the ribbon arrays was used.

**Electrical, morphological and optical characterization.** The electrical properties of the films were measured using the four-point method with a cascade Microtech 44/7 S 2749 probe station connected to a Keithley 2001 multimeter. Typically, six measurements were performed at different positions and the surface resistance was calculated with a standard deviation of 3.2%, 1.6% and 2.6% for the 3 nm, 6 nm and 15 nm gold films, respectively. The surface morphology was investigated by AFM (Bruker Dimension FastScan D3100) and field-emission SEM (Zeiss 1550VP). A field-emission transmission electron microscope (FEI Titan ChemiSTEM) was used in the STEM mode to collect high-angle annular dark-field images from a cross-section lamella prepared by in situ liftout technique using a dual beam instrument (FEI Quanta 3D 600 FEG). A pen mark (Sharpie marker) was applied to the coating surface for protection from focused ion beam (FIB) during the liftout. A spectrophotometer (Perkin Elmer LAMBDA 950) was used for optical spectra measurements in the visible and near-infrared wavelength ranges. Infrared spectra of the Au arrays were obtained with a Fourier-transform infrared spectrometer coupled to an infrared microscope (Bruker Tensor and Hyperion 2000). The light collection was limited to the nanoribbon array area using a knife-edge aperture in front of the infrared detector. An infrared polarizer was used to select a linearly polarized electric field oriented transversally to the nanoribbons to excite the plasmonic resonances. All measurements were performed in a nitrogen-purged atmosphere.

**Theoretical modelling of ultrathin metal films.** Following previous studies<sup>8,25</sup>, when the thickness *t* of UTMFs is above the percolation threshold, we write the Au dielectric function as  $\epsilon(\omega) = \epsilon_b(\omega) - \omega_p^2 / (\omega(\omega + i\Gamma/\hbar))$ , where the first term  $\epsilon_b(\omega)$  is a background permittivity associated with *d*-band transitions that becomes especially important at visible wavelengths, while the second term represents the conduction free-electron response. Here,  $\omega_p = \sqrt{4\pi n_b e^2 / m^*}$  is the bulk plasmon frequency,  $n_b$  is the bulk electron density,  $m^*$  is the effective electron mass, and  $\Gamma$  is the inelastic scattering rate, which is strongly dependent on the gold film thickness in our study. Following a previously introduced procedure<sup>10</sup>, we set the background permittivity to  $\epsilon_b(\omega) = \epsilon_{IC}(\omega) + \omega_0^2 / (\omega(\omega + i\Gamma_0/\hbar))$  (ref. <sup>36</sup>), where  $\epsilon_{IC}(\omega)$  are experimentally tabulated data<sup>37</sup>,  $\hbar\omega_0 = 9.06$  eV and  $\Gamma_0 = 0.071$  eV (ref. <sup>36</sup>). To characterize the quasi-two-dimensional nature of our sample, we can alternatively use an effective surface conductivity to describe its optical response as<sup>10,26</sup>  $\sigma_s(\omega) = \sigma_b(\omega) + (ie^2/m^*)n_s/(\omega + i\Gamma/\hbar)$ , where  $\sigma_b(\omega) = i\omega t(1 - \epsilon_b(\omega))/4\pi$  represents the effective background surface conductivity, and the second term is the Drude response associated with an effective surface charge density  $n_s = n_b t$ . In order to check the validity of our theoretical model, we present a comparison of transmission spectra for extended UTMFs of two different thicknesses in Supplementary Fig. 8. The discrepancy between experimental and theoretical results at *t* = 3 nm in this model could be attributed to the fact that we are using the nominal thickness in our theory, as well as to unaccounted-for damping effects. When doing calculations with *t* = 3.4 nm (close to the measured gold thickness; see TEM images in Supplementary Fig. 3), better agreement is obtained (blue dashed curve in Supplementary Fig. 8a).

## Data availability





All data needed to evaluate the conclusions in the paper are present in the main text and the supplementary materials. Any relevant information related to the study is available from the corresponding author upon reasonable request.

## References

- Leandro, L., Malureanu, R., Rozlosnik, N. & Lavrinenko, A. Ultrathin, ultrasmooth gold layer on dielectrics without the use of additional metallic adhesion layers. *ACS Appl. Mater. Interfaces* **7**, 5797–5802 (2015).
- Chen, C. F. et al. Controlling inelastic light scattering quantum pathways in graphene. *Nature* **471**, 617–620 (2011).
- Yu, R., Liz-Marzán, L. M. & García de Abajo, F. J. Universal analytical modeling of plasmonic nanoparticles. *Chem. Soc. Rev.* **46**, 6710–6724 (2017).
- Johnson, P. B. & Christy, R. W. Optical constants of the noble metals. *Phys. Rev. B* **6**, 4370 (1972).

In the format provided by the authors and unedited.

# Tunable plasmons in ultrathin metal films

Rinu Abraham Maniyara <sup>1,4</sup>, Daniel Rodrigo<sup>1,4</sup>, Renwen Yu <sup>1</sup>, Josep Canet-Ferrer<sup>1</sup>,  
Dhriti Sundar Ghosh<sup>1</sup>, Ruchirej Yongsunthon<sup>2</sup>, David E. Baker<sup>2</sup>, Aram Rezikyan<sup>2</sup>,  
F. Javier García de Abajo <sup>1,3\*</sup> and Valerio Pruneri <sup>1,3\*</sup>

---

<sup>1</sup>ICFO—Institut de Ciències Fotòniques, The Barcelona Institute of Science and Technology, Castelldefels (Barcelona), Spain. <sup>2</sup>Corning Research and Development Corporation, Sullivan Park, Corning, NY, USA. <sup>3</sup>ICREA—Institució Catalana de Recerca i Estudis Avançats, Barcelona, Spain. <sup>4</sup>These authors contributed equally: Rinu Abraham Maniyara, Daniel Rodrigo. \*e-mail: [javier.garciadeabajo@nanophotonics.es](mailto:javier.garciadeabajo@nanophotonics.es); [valerio.pruneri@icfo.eu](mailto:valerio.pruneri@icfo.eu)



# Supplementary Information

## Tunable plasmons in ultrathin metal films

Rinu Abraham Maniyara<sup>1</sup>†, Daniel Rodrigo<sup>1</sup>†, Renwen Yu<sup>1</sup>, Josep Canet-Ferrer<sup>1</sup>, Dhriti Sundar Ghosh<sup>1</sup>, Ruchirej Yongsunthon<sup>2</sup>, David E. Baker<sup>2</sup>, Aram Rezikyan<sup>2</sup>, F. Javier García de Abajo<sup>1,3\*</sup>, Valerio Pruneri<sup>1,3\*</sup>

### Affiliations:

<sup>1</sup> ICFO- Institut de Ciències Fotòniques, The Barcelona Institute of Science and Technology, 08860 Castelldefels (Barcelona), Spain

<sup>2</sup> Corning Research and Development Corporation, Sullivan Park, Corning, New York 14831, United States.

<sup>3</sup> ICREA- Institució Catalana de Recerca i Estudis Avançats, 08010, Barcelona, Spain.

† Equal contribution

\* Correspondence to: [valerio.pruneri@icfo.eu](mailto:valerio.pruneri@icfo.eu), [javier.garciadeabajo@nanophotonics.es](mailto:javier.garciadeabajo@nanophotonics.es)

### This file includes:

Supplementary note

Figs. 1 to 10

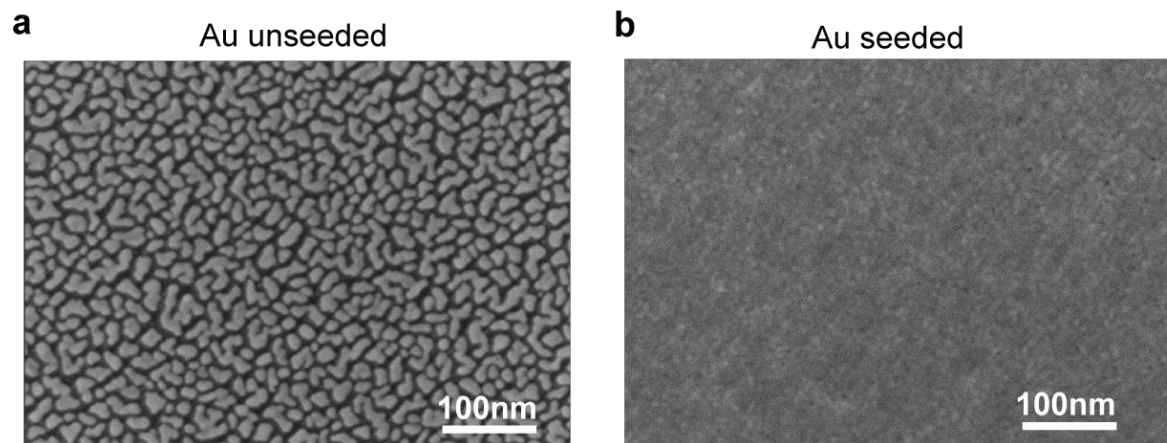
Table 1

Ref 38 to 42

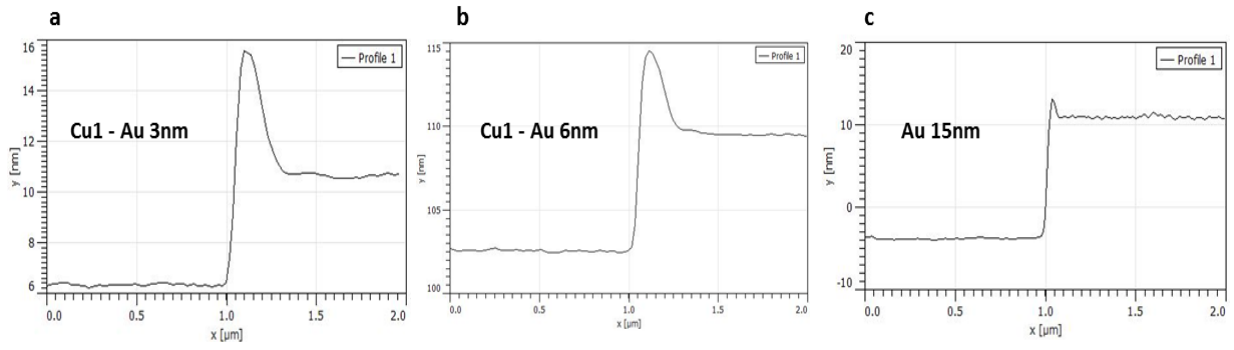
## **Supplementary note**

### **Wetting, electrical and optical effects of copper seed layer**

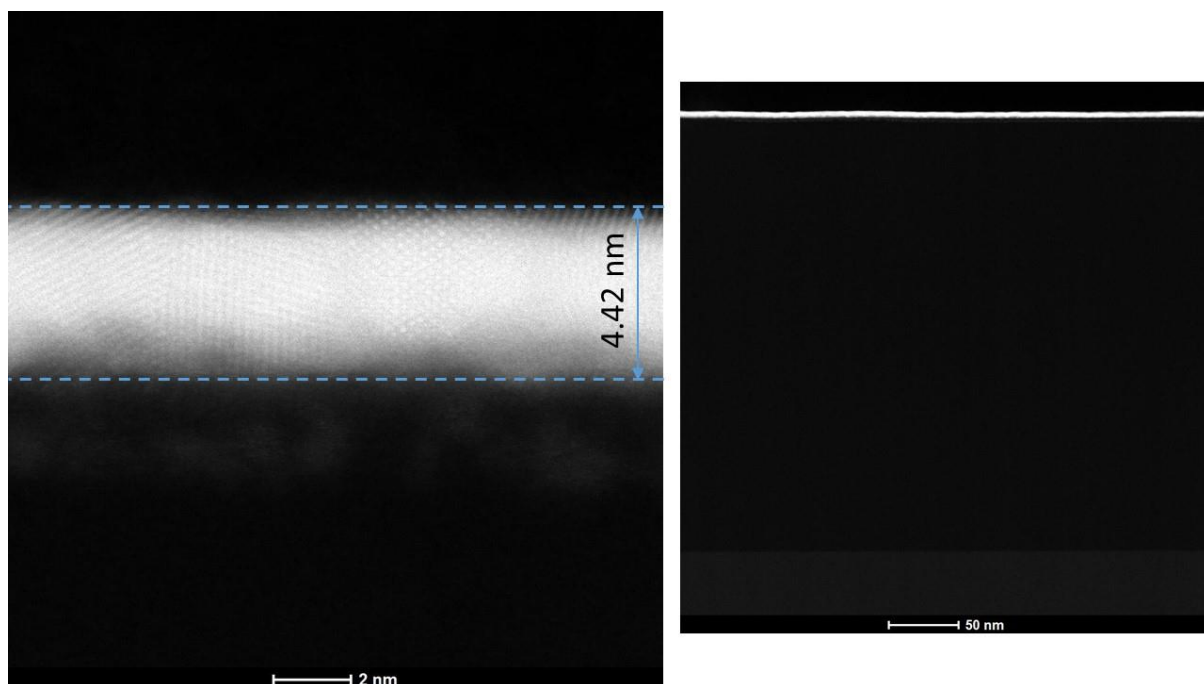
The copper seed layer used in the fabrication of the gold UTMFs has a significant wetting effect on the morphology of the gold layer, as it leads to percolation at nominal thicknesses (1 nm) much lower than the unseeded case (7 nm). However, we believe that the contribution of the copper seed layer to the electrical and optical conductivity should be negligible. AFM and SEM images indicate that the copper seed layer is composed of disconnected islands with a lateral size of the order of 10-20 nm, which is further corroborated by the fact that it is not electrically conductive. The copper seed layer islands are likely to undergo oxidation, as they remain exposed to air (ambient atmosphere) before gold deposition<sup>38</sup>. This is consistent with optical measurements, where transmission, reflection and absorption qualitatively are similar to copper oxide, with no sign of any characteristic metal particle response, in contrast to an equal mass-equivalent thickness (1 nm) of unseeded gold that clearly shows peaks in the optical response associated with localized optical modes. We have also performed time-of-flight secondary-ion-mass spectroscopy (TOF-SIMS) measurements. The thickness of the copper seeded gold films is slightly larger than the nominal values (by 10.5% and 5.7 % for the 3 and 6 nm gold films seeded by copper, respectively), which are likely attributable to the formation of oxide as this has a volume larger than the original metal (68% increase from Cu to Cu<sub>2</sub>O).



**Supplementary Fig. 1** Scanning Electron Microscope image of nominal thickness  $t=3$  nm **a**, unseeded and **b**, seeded gold film grown on 285nm thick native silica oxide on Silicon substrate. Unseeded gold grows with discontinuous island-like morphology, while the seeded gold is percolated (see also AFM images of Fig. 1 in the main text).

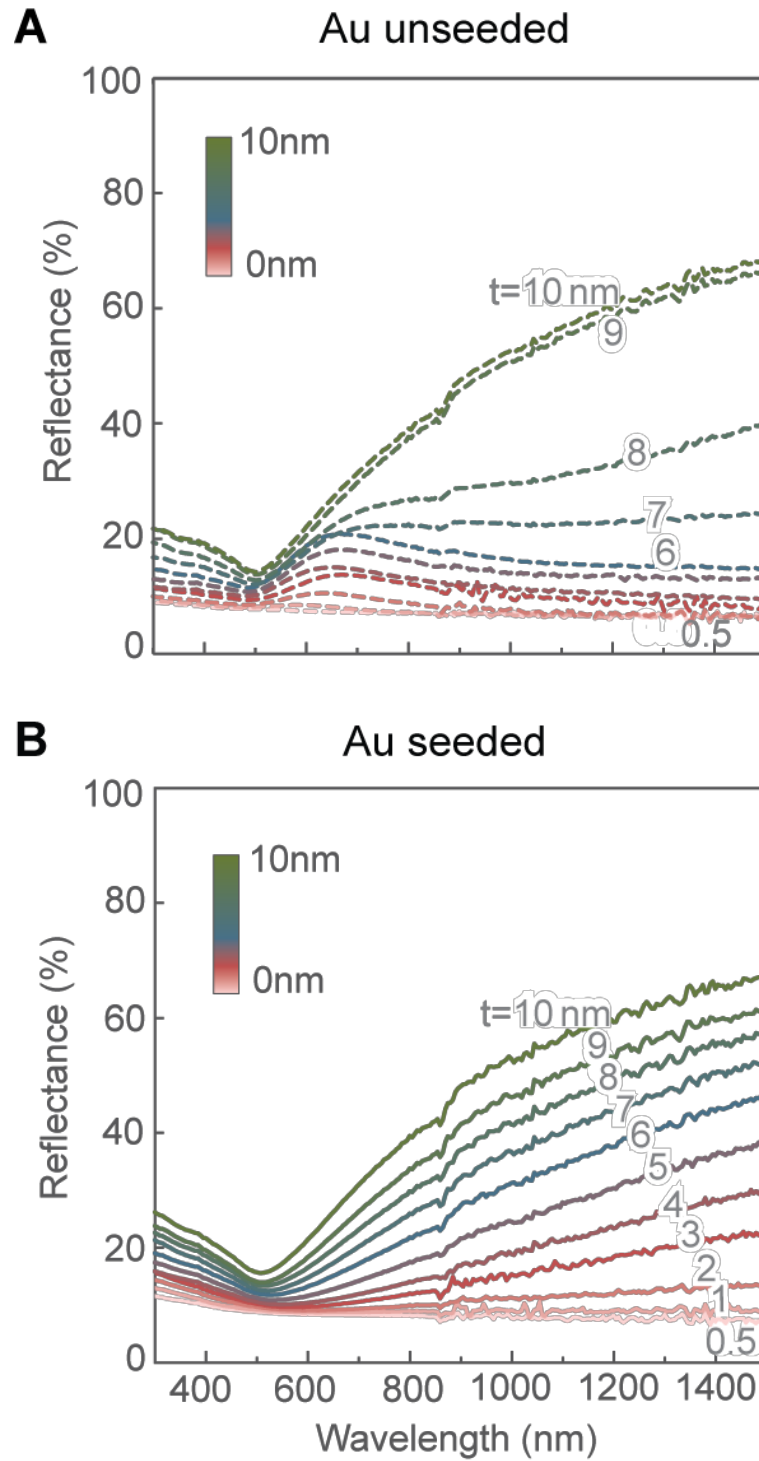


**Supplementary Fig. 2** Atomic force microscope (AFM) profiles for **a**,  $t=3$  nm and **b**, 6 nm gold seeded with 1 nm copper. For comparison we add also a scan for **c**,  $t=15$  nm unseeded gold. The geometrical thicknesses in these plots (y axis) is calculated from 20 cross sectional measurements and their average values are  $4.42 \pm 0.14$ ,  $7.40 \pm 0.16$  and  $14.87 \pm 0.18$  nm, respectively, in the plateau beyond the elevation peaks observed near the edge of the Au film. Note that each AFM point is an average of 20 pixels and the roughness is not properly resolved in these profiles. Instead, the AFM measurements reported in Fig. 1 of the manuscript, that gave  $R_q=0.22$  nm for  $t=3$  nm seeded gold, were obtained on a much smaller scan area ( $500 \times 500$  nm<sup>2</sup>) with a lateral resolution of 3 nm, smaller than that used in these profile measurements ( $<7$  nm).

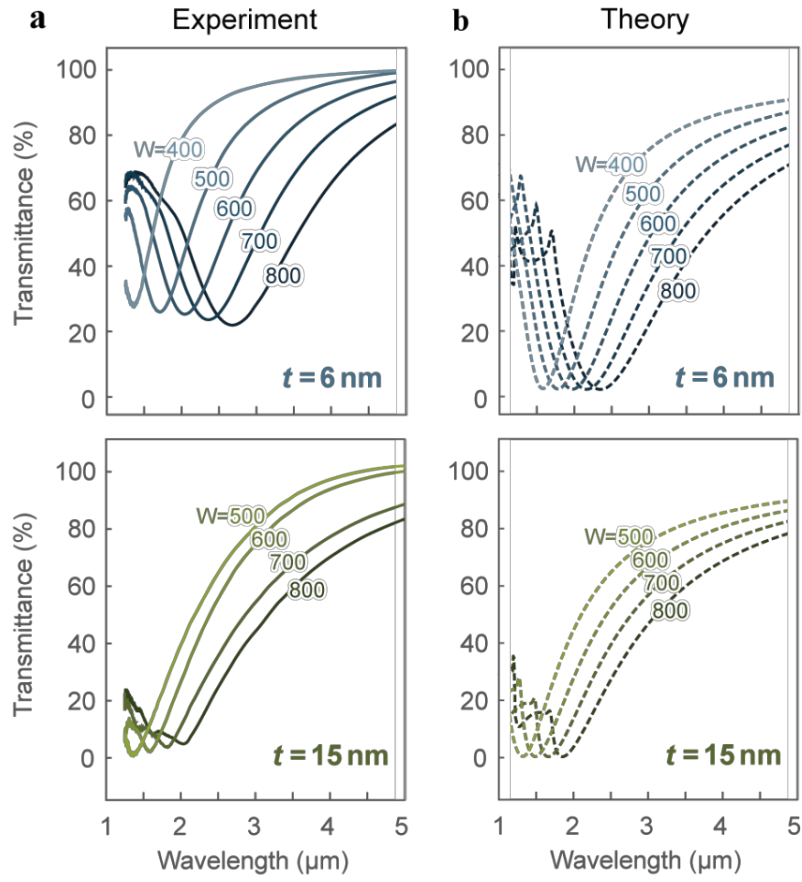


**Supplementary Fig. 3** Scanning Transmission Electron Microscope (STEM) images of nominal thickness  $t=3$  nm gold film seeded by 1 nm copper, grown on 285 nm thick native silica oxide on silicon substrate. The average geometrical thickness of  $4.42 \pm 0.14$  nm measured by AFM is indicated as an eye guideline, showing agreement between STEM and AFM measurements. HAADF STEM images were recorded with 200 keV electrons at sub-angstrom resolution. Scale bar: 2 nm (left image) and 50 nm (right image).

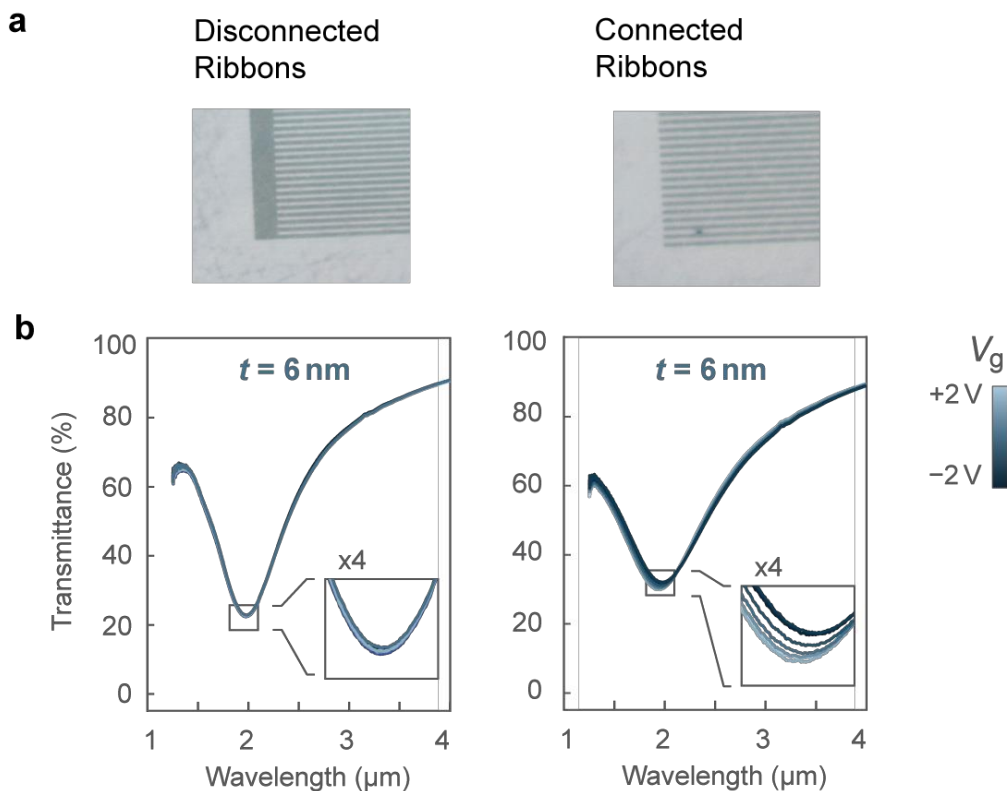




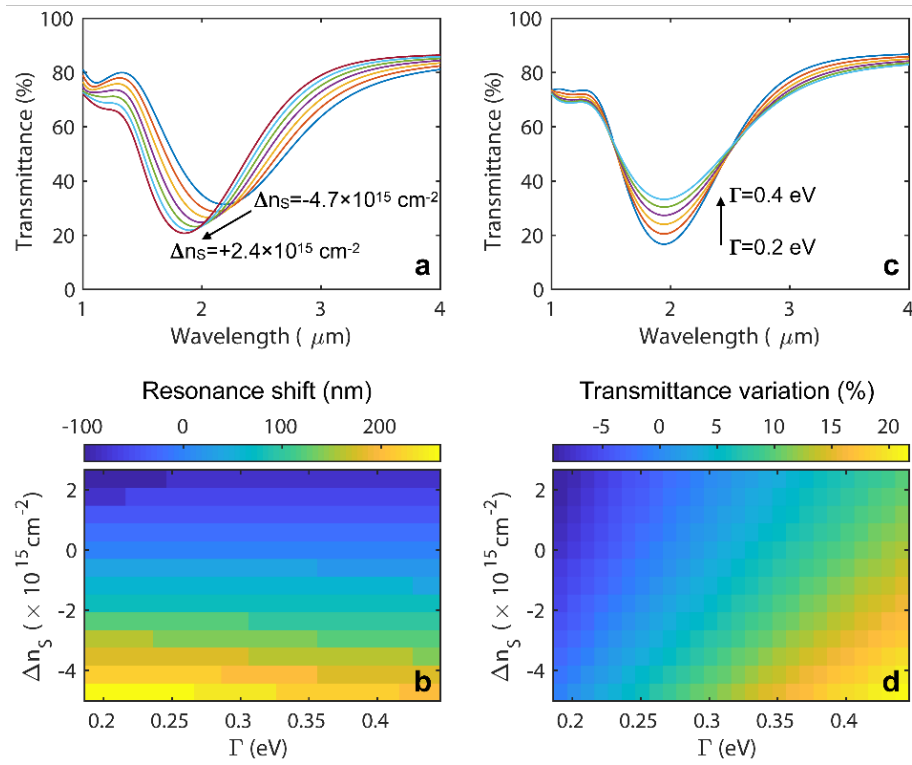
**Supplementary Fig. 4** Near-infrared and visible reflectance spectra of **a**, unseeded and **b**, seeded UTMFs for different nominal gold thicknesses  $t$ . The spectra of the unseeded gold UTMFs show a reflection peak at around 600 nm for  $t < 7$  nm, which can be attributed to resonances of isolated gold islands, indicating a disconnected layer. The spectra of the seeded gold UTMFs show progressively increasing reflection at near-infrared wavelengths for  $t \geq 1$  nm, demonstrating long-range connectivity. In contrast, the reflectance of the seeded gold UTMFs confirms percolation of the film already at  $t = 1$  nm. Note that the larger noise for wavelength larger than about 850 nm is associated with a change in the illumination lamp.



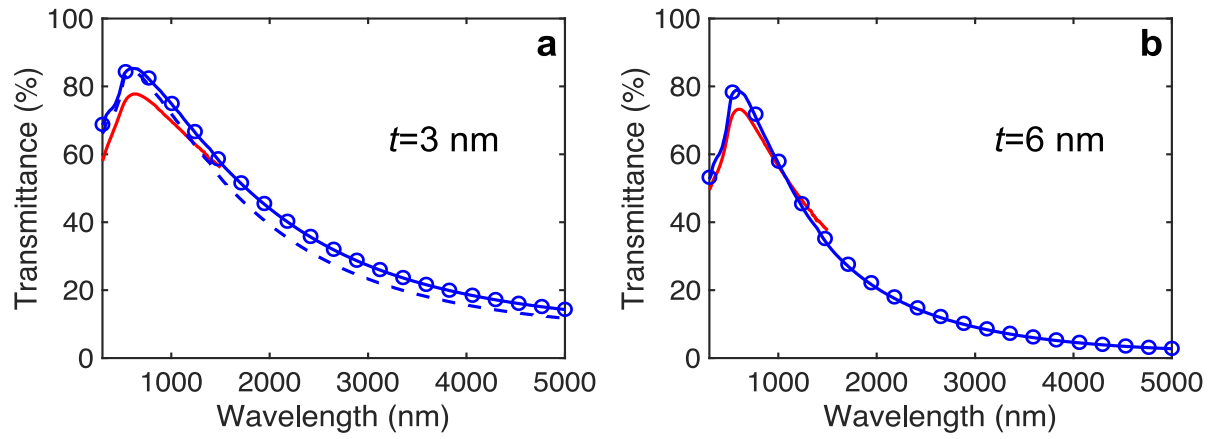
**Supplementary Fig. 5** **a**, Experimental and **b**, simulated transmittance spectra of the seeded gold UTMF nanoribbons showing plasmonic resonances from the near- to the mid-infrared for different ribbon widths  $W$  and nominal thickness  $t=6$  nm and  $t=15$  nm. A gold Drude model with  $\Gamma=0.10$  eV and  $\Gamma=0.07$  eV has been used in these simulations for  $t=6$  nm and  $t=15$  nm, respectively. Similar results can be also obtained with larger values of the damping.



**Supplementary Fig. 6 a**, Optical microscope images and **b**, experimental transmittance spectra of seeded gold UTMF nanoribbons disconnected and connected to the external electrical gate for different bias voltages  $V_g$ . The connected and disconnected arrays have identical dimensions ( $W=500 \text{ nm}$ ,  $t=6 \text{ nm}$ ), are located on the same chip and covered by the same ion gel layer. The plasmonic resonance of the array connected to the external gate is electrically tuned with the bias voltage, while the resonance of the disconnected array remains unmodified for all gating voltages.

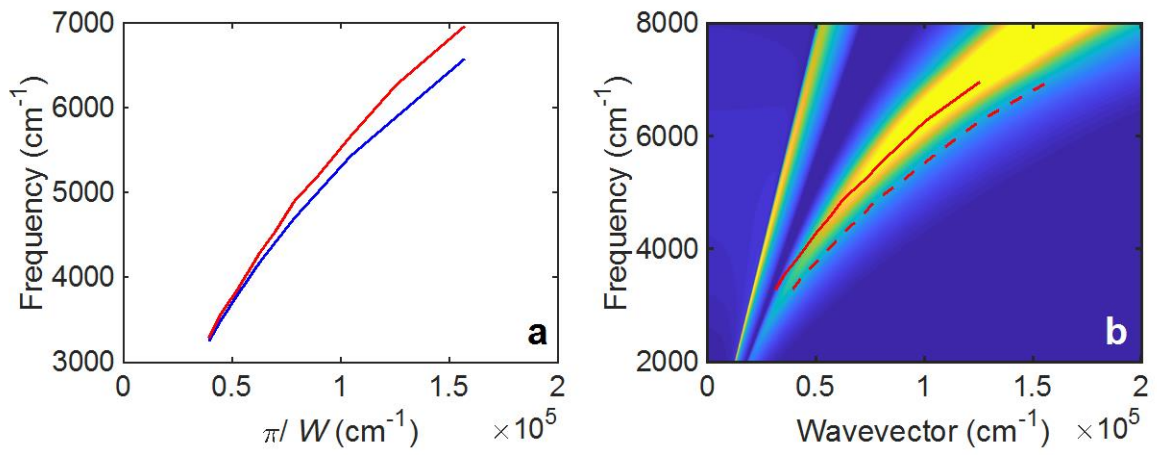


**Supplementary Fig. 7** Simulated transmission spectra of gold UTMF nanoribbon array having thickness  $t=3$  nm and width  $W=500$  nm. The transmission spectra are plotted for different effective surface charge density variations  $\Delta n_s$  (a) and for different metal damping rates  $\Gamma$  (c). Color plots represent the wavelength shift (b) and transmittance variation (d) of the plasmonic resonance as a function of effective surface charge density variation  $\Delta n_s$  and metal damping rate  $\Gamma$ . The wavelength shift in these calculations is almost entirely produced by the effective surface charge density variation  $\Delta n_s$ . The transmittance variation  $\Delta T$  is mostly produced in these simulations by changes in the metal damping rate  $\Gamma$  and, to a lower extent, by the effective surface charge density variation  $\Delta n_s$ . The effective surface carrier density change, used as a fitting parameter, does not necessarily correspond to a change of bulk carrier density (number of electrons per unit volume) induced in the metal.

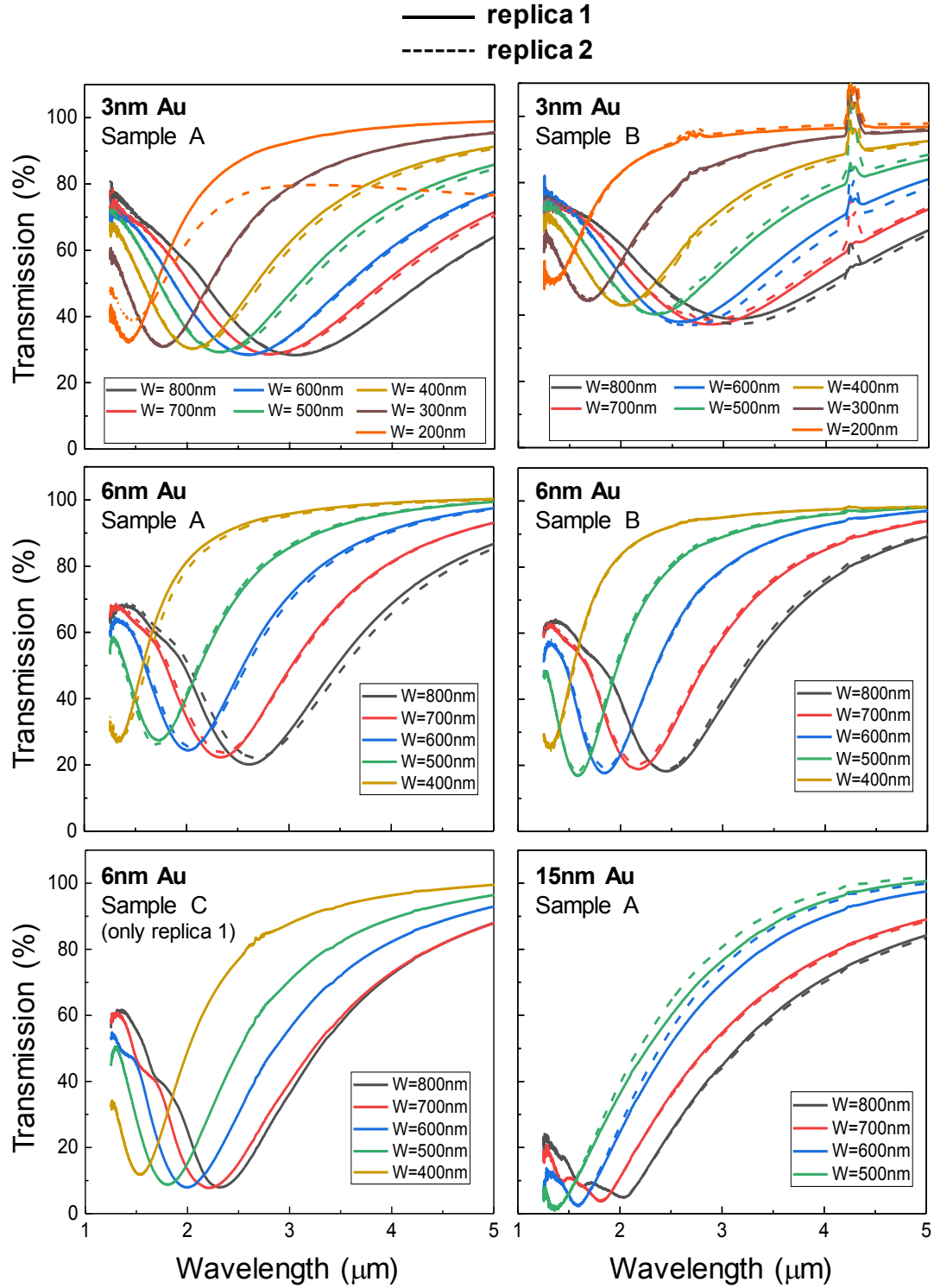


**Supplementary Fig. 8** Comparison of transmission spectra for extended UTMFs of two different nominal gold thicknesses:  $t=3$  nm in **a** and  $t=6$  nm in **b**. Blue-solid curves represent calculated results using the bulk permittivity  $\epsilon(\omega)$ , while blue circles represent calculated results using the effective surface conductivity  $\sigma_s(\omega)$ . Red curves are measured spectra taken from Fig. 1 of the main manuscript. The blue-dashed curve in **a** are calculations for  $t=3.4$  nm.





**Supplementary Fig. 9 a**, Comparison of experiment (red-solid curve) and theory (blue-solid curve) results extracted from Fig. 2c of the main manuscript for the resonance positions of localized surface plasmons in ultrathin gold ribbons (nominal thickness  $t=3$  nm) with different nominal widths  $W$ . The observed minor discrepancy could be due to fabrication imperfections. **b**, Same as Fig. 2f of the main manuscript but comparing the measured results using both a wave vector  $\pi/W$  (red-dashed curve) and an effective wave vector  $\pi/1.25W$  (red-solid curve).



**Supplementary Fig.10**, Plots of the transmission spectra obtained from all of our successfully measured chips with the same period-to-width ratio (period equal to 1.5 times the ribbon width). Each panel corresponds to a different chip. Two replicas within each chip have been obtained for all chips except one. The nominal gold thickness (mass-equivalent deposition) is indicated by labels. All other experimental parameters are the same as in Fig. 2c of the main text.

**Supplementary Table. 1**

Reference	Mechanism of thin film formation	RMS Roughness (nm)	Percolation thickness of Au (nm)	Limitations
<sup>29</sup>	surface treatment with (3-mercaptopropyl) trimethoxysilane		5.4	Sample preparation takes 1 week, higher deposition rate must be used (10A°/S) for thermal evaporator
<sup>36</sup>	surface treatment with aminosilanes	below 0.3	6	Surface treatment takes 3 h, Au deposition should be done as soon as after treatment since adhesion promoter is reactive, needs higher deposition rate
<sup>39</sup>	Chemical mechanical polishing	0.3		Top ~4 nm of gold is removed during polishing
<sup>40</sup>	Galvanic displacement	0.35		Thickness control is difficult
<sup>41</sup>	Template stripping	0.2		Longer, complicated procedure
<sup>42</sup>	Surface coated with CYCLOTENE polymer		3-4	High sheet resistance for thinner films
Our work	Cu metal seed layer	0.2 - 0.3	1	

**Supplementary Table 1** Comparison of different works carried out to fabricate ultrathin gold films. The mechanism of thin film formation, RMS roughness, percolation thickness, and limitations of the works are taken into consideration.

38. Zuo, Z.J., Li, J., Han, P.D., Wang, W. XPS and DFT Studies on the Autoxidation Process of Cu Sheet at Room Temperature. *J. Phys. Chem.* **118**, 35, 20332-20345 (2014).
39. Miller, M. S., Ferrato, M. A., Niec, A., Biesinger, M. C. & Carmichael, T. B. Ultrasooth gold surfaces prepared by chemical mechanical polishing for applications in nanoscience. *Langmuir* **30**, 14171–14178 (2014).
40. Gutés, A., Carraro, C. & Maboudian, R. Ultrasooth gold thin films by self-limiting galvanic displacement on silicon. *ACS Appl. Mater. Interfaces* **3**, 1581–1584 (2011).
41. Chai, L. & Klein, J. Large area, molecularly smooth (0.2 nm rms) gold films for surface forces and other studies. *Langmuir* **23**, 7777–7783 (2007).
42. Leosson, K. *et al.* Ultra-thin gold films on transparent polymers. *Nanophotonics* **2**, 3–11 (2013).